The Relation between Jet Meandering and Storm Intensity in an Idealized Aquaplanet GCM

EREZ AVIV[a] AND YOHAI KASPI[a]

[a] *Department of Earth and Planetary Sciences, Weizmann Institute of Science, Rehovot, Israel*

(Manuscript received 29 August 2024, in final form 6 October 2025, accepted 1 November 2025)

ABSTRACT: The eddy-driven jet meandering has been hypothesized to increase due to climate change. This meandering frequently relates to slow-moving patterns of surface low and high pressure anomalies, potentially causing extreme weather events such as droughts, flooding, heat waves, and cold spells. However, the quantitative link between jet meandering and storm development is still lacking, as well as a conclusive mechanism for the effect of climate change on jet meandering. In this study, we separate the physical components in the atmospheric complex system using an idealized moist global circulation model (GCM), performing a series of global warming simulations. We outline the connection between the decreasing equator-to-pole temperature gradient due to Arctic amplification and the meandering of the jet. We derive a theoretical relation between the 500-hPa geopotential height meridional gradient and jet meandering, indicating that the leading reason for the increase in jet meandering is the flattening of the midatmospheric meridional temperature gradient, constraining the variations of the streamfunction anomaly with latitude. As it decreases, the eddy-driven jet slows and its meridional layout widens. By Lagrangian tracking of cyclones and anticyclones, we link the jet meandering to the development of cyclones and anticyclones, showing that intense storms are more likely to be associated with jet meanders during their development stage. Furthermore, jet stream meanders with greater meridional extent will be more likely associated with intense storms. In simulations with increased mean surface temperature, our results demonstrate an increase in both jet meandering and storm intensity.

KEYWORDS: Dynamics; Rossby waves; Extratropical cyclones; Extreme events; Jets; Climate change

1. Introduction

The eddy-driven jet plays a prominent role in large-scale dynamics, advecting momentum, heat, and moisture in the midlatitudes. The jet frequently meanders in a wavy pattern, manifested as synoptic Rossby waves, forming high and low pressure anomalies along the flow (Rhines 1975; Vallis 2017; Chen et al. 2022). Midlatitude weather extremes such as droughts, floods, heat waves, and cold spells are induced within the flow and influenced by it (e.g., Dole et al. 2011; Barnes 2013; Screen and Simmonds 2013, 2014; Röthlisberger et al. 2016). However, how much of the midlatitude extreme weather events are related to the jet meandering is yet to be quantified. Moreover, in recent years, there has been a growing debate about whether there will be an increase in the jet meandering in a changing climate and how it will affect extreme weather events frequency, intensity, and duration (e.g., Francis and Vavrus 2012; Barnes 2013; Hassanzadeh et al. 2014; Chen et al. 2015; Robert et al. 2019; Blackport and Screen 2020; Kornhuber et al. 2020; Sun et al. 2022). This study aims to quantify the fundamental relation between the eddy-driven jet meandering at upper levels and extratropical extreme storm intensity at the surface and to examine the effect of climate change on both phenomena.

Arctic amplification (AA) refers to the enhanced warming in the Arctic relative to lower latitudes in response to the increased atmospheric greenhouse gas concentrations. This enhanced warming is primarily driven by temperature feedback, where more energy is radiated back to space in low latitudes than in high latitudes, as well as by the sea ice loss feedback, which reduces surface albedo and further amplifies warming (e.g., Manabe and Stouffer 1980; Serreze et al. 2009; Pithan and Mauritsen 2014; Previdi et al. 2021). Francis and Vavrus (2012) suggested that AA would lead to a slower eastward progression of Rossby waves in the mid- to upper-atmospheric levels and persistent weather patterns in autumn and winter. By analyzing observational data, they provided two optional mechanisms linking AA to the persistence of weather conditions. The first is a weakened meridional gradient in the 500–1000-hPa atmospheric column thickness, and the second is a northward elongation of ridge peaks at 500-hPa waves. They argued that these changes reduce zonal jet speed and enhance jet meandering, thereby increasing the likelihood of prolonged, extreme weather events such as maximum temperature extremes. However, they did not explicitly examine how these responses relate to the intensity of extratropical storm systems.

Using a different metric to analyze the observational geopotential height contours, Barnes (2013) claimed that Francis and Vavrus's (2012) observations of planetary wave elongation might be an artifact of their methodology. Moreover, she showed a complex linkage between the 500-hPa westerly speed and the wave phase speed. While the former is decreasing, the latter has the opposite trend in the autumn and winter seasons. From a blocking event perspective, she found no statistically significant increase in blocking frequency over all seasons. With no alternative observational analyses and simulations supporting Francis and Vavrus' hypothesis, Wallace et al. (2014) claimed their linkage between extreme cold-air outbreaks

Corresponding author: Erez Aviv, eaviv8@gmail.com

DOI: 10.1175/JCLI-D-24-0444.1

and global warming is only by coincidence. Using an idealized dry global circulation model (GCM), Hassanzadeh et al. (2014) analyzed the response of jet meandering, quantified by Rossby wave amplitude, and blocking frequency, to AA. They found that a reduced meridional temperature gradient decreases both wave amplitude and blocking frequency, in contrast to the hypothesis of Francis and Vavrus (2012). Recent studies, such as Martin (2021), find a robust and statistically significant increase in the meandering of the polar jet during boreal winter, particularly over the Pacific sector. In contrast, using observational data, Overland et al. (2021) argue that intermittency and the presence of overlapping processes, such as internal variability, make it difficult to isolate the AA signal. Geen et al. (2023) show that the apparent contradictions across studies can often be attributed to metric dependence, i.e., different methods for quantifying jet meandering yield different trends. Likewise, Nie et al. (2023) show that while models generally agree on AA and a reduced meridional temperature gradient, they diverge in their predictions of circulation changes, stressing the need for better observational constraints to narrow model uncertainty. The divergent findings across these and other studies further highlight the complexity of diagnosing changes in jet meandering (e.g., Screen and Simmonds 2013; Barnes and Polvani 2015; Francis and Vavrus 2015; Di Capua and Coumou 2016; Cattiaux et al. 2016; Peings et al. 2018; Cohen et al. 2020; Dai and Song 2020).

The reduction in the meridional temperature gradient associated with AA has been proposed as a key driver of changes in the Northern Hemisphere (NH) eddy-driven jet, potentially slowing its circulation (Francis and Vavrus 2012). However, observed and projected responses of the NH eddy-driven jet and storm tracks exhibit seasonal differences. In boreal summer, when meridional temperature gradients are weaker, the effects of AA on the eddy-driven jet are less pronounced. Yet, a weakening of the jet and storm tracks has been observed, with future projections suggesting further weakening and increased persistence of weather extremes (e.g., Coumou et al. 2015; Harvey et al. 2020; Chemke and Coumou 2024). In contrast, winter observations and projections indicate a strengthening of the jet, with storm tracks shifting poleward and weakening in response to the reduced baroclinicity (Harvey et al. 2014; Tamarin and Kaspi 2017a; Blackport and Fyfe 2022). It is important to note that trends in storm-track intensity do not necessarily translate to changes in individual storms, as single-storm intensity and storm-track intensity can respond differently (e.g., Chang and Guo 2012; Priestley and Catto 2022). Projected changes in the NH eddy-driven jets location vary by season. During summer, a clear poleward shift is anticipated, whereas in winter, the response differs by region. The Pacific jet is expected to shift poleward robustly, while the North Atlantic jet exhibits a less pronounced displacement (Afargan and Kaspi 2017; Ossó et al. 2025).

The response of the eddy-driven jet to climate change is influenced by multiple competing factors, leading to complex changes in the atmospheric circulation. Butler et al. (2010) highlighted that while AA drives a poleward shift of the jet and storm tracks, upper-tropospheric warming in the tropics induces an equatorward shift. Additionally, cooling in the polar stratosphere further complicates the overall response (e.g., Shaw et al. 2016; Chen et al. 2020). A key aspect of this response is the interplay between changes in the meridional temperature gradient at different atmospheric levels. While AA reduces the surface meridional temperature gradient, potentially increasing jet meandering, upper-tropospheric warming strengthens the temperature gradient at higher altitudes, which can suppress meandering (e.g., Robert et al. 2019; Nie et al. 2022). Yuval and Kaspi (2020) demonstrated that the impact of upper-level temperature gradients on eddy activity and zonal wind is comparable in magnitude to that of the reduced surface gradient. Furthermore, changes in atmospheric static stability must also be considered, as they significantly influence eddy activity and storm development (e.g., Lu et al. 2008). By applying numerical simulations in an idealized GCM setting, Moon et al. (2022) further proposed that zonally asymmetric factors play a key role in the relationship between AA and jet meandering, underscoring the need to consider regional processes such as land–ocean thermal contrast or orographic forcing. Considering these effects, comprehensive climate models generally project a decrease in jet meandering and atmospheric blocking events in a warming climate (Peings et al. 2018; Barnes and Polvani 2015). However, using the local wave activity (LWA) metric to assess the jet meandering, Chen et al. (2022) suggested that increased wave activity in boreal winter in the changing climate results primarily from a weakened jet as a mixing barrier for eddy transport rather than changes in eddy phase speed, as postulated before. Using full climate models, Chemke and Coumou (2024) found that climate models project a weakening of storm tracks in boreal summer, potentially leading to more persistent weather conditions that can develop into extreme weather events.

The connection between blocking events, a persistent Rossby wave ridge or trough that disrupt the westerly flow, and extreme weather events has been extensively studied (Pfahl and Wernli 2012; Brunner et al. 2018; Wolf et al. 2018; Woollings et al. 2018). In a baroclinic region, an upper-level vorticity anomaly caused by the jet's meandering induces a lower-level anomaly, which reinforces the upper anomaly and slows its eastward progression (Hoskins et al. 1985; Vallis 2017). Screen and Simmonds (2014) looked at extreme weather months and found that significantly amplified midtropospheric Rossby waves commonly accompany them. The findings point to a causal link between amplified waves and surface temperature anomalies, suggesting that this would increase the probability of extreme events in a changing climate where quasi-stationary waves are amplified. Using theoretical arguments, Hoskins and Woollings (2015) suggested an increase in surface temperature anomalies with the increase in Rossby wave amplitude, leading to an increase in the latent heat released in a cyclone and its intensity. They also claim that the weakening of the zonal flow due to AA will increase the stationary Rossby waves' wavenumber. Using reanalysis data, Kornhuber et al. (2020) found that amplified Rossby waves with wavenumbers 5 or 7 during NH summer increase the probability of getting more concurrent heat extremes, highlighting the strong influence of jet structure on midlatitude weather persistence. However, whether

increased jet meandering, reflected in 500-hPa wave amplitude, enhances storm intensity remains unclear. For example, Sinclair et al. (2020) found that rising mean sea surface temperatures intensified strong cyclones in an idealized model, but they did not assess the role of jet meandering. Recently, Tamarin-Brodsky and Harnik (2024) investigated the connection between Rossby wave breaking and weather extremes in the North Atlantic during winter and found that, in most cases, there has been an association with upper-level Rossby wave breaking. They showed a correlation between the cyclone's or anticyclone's position relative to the Rossby wave breaking, pointing to a preferred position for intense storms. While there is an apparent connection between jet meandering and extreme events, the percentage of storms associated with jet meanders in space and time, as well as the effect of larger jet meandering on storm intensity, has yet to be systematically quantified.

In this study, we examine the links between global warming and changes in storm intensity. Global warming is hypothesized to weaken jet velocity, causing the jet stream to meander more and thereby increase the persistance of weather systems. While Francis and Vavrus (2012) focused on blocking events, we examine and quantify the effect of jet meandering changes on cyclones and anticyclones. Using a combination of an idealized moist GCM and Lagrangian tracking, we analyze changes in jet speed and meandering, along with quantifying the amount of storms generated or intensified as a result of jet meanders. The idealized GCM enables us to isolate the physical effects of a decrease in meridional temperature gradient on jet meandering and its influence on storms. At the same time, the Lagrangian approach allows us to track jet meanders, upper-level vorticity anomalies, and storm development, revealing their causal link. By quantifying the meridional extent of each ridge and trough in the jet, we can establish a connection between storm intensity to the extent of the jet meander. Applying the algorithm over a large dataset of jet meanders and storms ensures statistical robustness. Additionally, we derive a theoretical relation between a reduction in the 500-hPa geopotential height meridional gradient and an increase in jet meandering, providing insight into the link between the two processes.

This paper is organized as follows: Section 2 describes the coupling methodology between idealized moist GCM simulations and the Lagrangian storm-tracking algorithm. We also present our two-step process for quantifying the association between storms and upper-level jet meandering, along with the metrics we use to measure the eddy-driven jet meridional elongation. Section 3a examines how jet meandering changes with rising mean surface temperature. In section 3b, we demonstrate that this change is linked to a reduction in the meridional temperature gradient, which leads to a decrease in jet speed and a change in jet meandering. In section 3c, we quantify the link between jet meandering and storm intensity and discuss its effect on the increased intensity of storms in global warming simulation. Section 4 summarizes the results.

2. Methods

We use an idealized moist aquaplanet GCM based on the Geophysical Fluid Dynamics Laboratory (GFDL) Flexible Modeling System (FMS) framework. The model uses an Eulerian spectral dynamical core to solve the three-dimensional, hydrostatic primitive equations and thermodynamic equation for an ideal-gas atmosphere (Frierson et al. 2006; Anderson et al. 2004; O'Gorman and Schneider 2008; Jeevanjee et al. 2017; Yuval and Kaspi 2020; Feldl and Merlis 2021). Its lower boundary is a mixed layer ocean surface with a depth of 1 m. It is an energy-conserving layer with a specified heat capacity but no prescribed heat uptake or ocean heat transport. The surface temperature is determined by surface heat fluxes of radiative energy and latent and sensible heat. The model has no seasonal or diurnal cycle and is forced by a constant solar insolation corresponding to perpetual equinox conditions. A two-stream gray radiation scheme is used, and radiation fluxes are a function of temperature only. The shortwave radiation is a function of latitude only, with no solar radiation absorbed in the atmosphere. It is idealized as specified heating of the surface with surface albedo included inside of it. The solar flux is formulated by $R_S = (1/4)R_{S0}[1 + (\Delta_s/4)(1 - 3\sin^2\theta)]e^{-\tau_s\sigma^2}$, where $R_{S0} = 1360$ W m^{-2} is the global mean net solar flux, $\Delta_s = 1.2$ is the latitudinal variation of shortwave radiation, $\tau_s = 0.08$ controls the vertical absorption of solar radiation in the atmosphere, and θ is the latitude. The longwave optical depth τ depends on latitude and pressure, according to Eq. (1):

$$\tau = [f_l\sigma + (1 - f_l)\sigma^4][\tau_e + (\tau_p - \tau_e)\sin^2\theta], \quad (1)$$

where $\sigma = p/p_s$ is the vertical coordinate (p_s is the surface pressure and p is the pressure), $f_l = 0.2$ is the linear optical depth parameter, and $\tau_e = 8.2$ and $\tau_p = 2.4$ are the longwave optical thicknesses at the equator and the pole, respectively, in the reference simulation with Earth-like temperature distribution (O'Gorman and Schneider 2008; Tamarin and Kaspi 2016). The model has simplified moist convection and condensation schemes, with water vapor as a prognostic variable. As it exceeds saturation in a grid point, it condenses and falls out immediately but reevaporates below. Hence, no clouds exist, and changes in water vapor do not directly affect the radiative transfer. For a detailed description of the model, see Frierson et al. (2006). The spectral resolution we use is T85, corresponding to a horizontal grid resolution of 1.4° × 1.4°, and 30 vertical sigma levels. The model does not include clouds, ice, and chemical processes. However, it still obtains the leading order features of Earth's climate (Kaspi and Showman 2015).

a. *Tracking method*

We apply a Lagrangian feature point-tracking algorithm to track cyclones and anticyclones on the GCM output relative vorticity field. The algorithm identifies and characterizes the extratropical eddies on the sphere after removing the background field to isolate the synoptic and mesoscales (Hodges 1995). Here, we identify vorticity anomalies using the 850-hPa (lower level) and 300-hPa (upper level) vorticity fields and then track their centers every 6 h. A cutoff of $|10^{-5}|$ s^{-1} is used, and only extratropical NH vorticity anomalies that last more than 2 days are analyzed. Lower-level positive (negative) anomalies, indicating cyclones (anticyclones), initiated between latitudes $20° \le \theta \le 70°$ are referred to as extratropical

storms. The identified storms in each simulation are classified into five intensity levels based on their maximum intensity. This classification is determined using percentiles, with each level representing a 20th percentile range, where the most intense storm in the simulation corresponds to the 100th percentile. The intensity levels are defined separately for cyclones and anticyclones, regardless of their spatial location. This approach ensures a systematic comparison of storms across different intensity levels while maintaining consistency across simulations.

With the GCM simulations and tracking algorithm output, we have an extensive dataset of storms and jet meanders, which allows us to quantify their relation. Several spatial and temporal factors need to be considered to associate lower-level storms, which give rise to weather phenomena, with upper-level jet meanders. During the growing stage of a baroclinic wave, its phase will be tilted westward with height. Consequently, the upper-level vorticity anomaly will not be vertically aligned over the lower-level vorticity anomaly but shifted to the west. Additionally, due to the NH meridional temperature gradient, the lower-level cyclonic (anticyclonic) motion causes temperature advection poleward (equatorward) east of the circulation center. Thus, it shifts the location of the lower-level maximum vorticity anomaly meridionally (Hoskins et al. 1985). Furthermore, there may be a time lag between the appearance of the upper-level vorticity anomaly due to jet meandering and the time of the lower-level maximum vorticity anomaly.

We develop a two-step process to directly associate 850-hPa lower-level storms (surface storms hereafter) with the corresponding 300-hPa geopotential height ridges and troughs. Figure 1 shows a snapshot of the association process between surface cyclone (anticyclone) and trough (ridge) in the eddy-driven jet.

1) We take a box at the 300-hPa pressure level sized 10° in longitude by 16° in latitude with the maximum intensity of surface cyclones (anticyclones) positioned at the center of the eastern side of the box (red dashed box in Fig. 1), and look for any cyclonic (anticyclonic) motion found by the tracking algorithm within the box. To ensure we analyze only lower- and upper-level vorticity anomalies that interact and intensify each other, we move the box with the center of the surface storm for 12 h before and after its maximum intensity. If such an upper-level vorticity anomaly is found, for all 24 h, then the surface storm is considered associated with an upper-level vorticity anomaly.
2) We take another box at the 300-hPa pressure level, sized 20° in longitude by 8° in latitude, centered around the location of the upper-level vorticity anomaly (blue dashed box in Fig. 1). For each 300-hPa isopleth, we identify its local minimum (troughs) and maximum (ridges) latitudinal points and assess whether any are located within the box. The isopleth with the point closest to the anomaly center is selected. A surface cyclone (anticyclone) is considered associated with a jet meander if such a trough (ridge) is found.

The criterion that the storm's peak intensity occurs close in time and space to a geopotential height ridge or trough is essential to ensure a physical interaction between the geopotential height excursions, upper-level vorticity anomalies, and surface storms. The box sizes in the two-step association algorithm were chosen based on key physical considerations. For the first step, we accounted for the typical size of a surface storm, meridional temperature advection, and westward vertical shift of the pressure anomalies during extratropical storm development. For the second step, we based the box size on an averaged scale of 300-hPa geopotential height ridges and troughs, assuming that vorticity anomalies develop near the maximum pressure anomaly (jet meander's peak). Note that the box size used to associate between upper-level vorticity anomaly and jet meander is much smaller in the meridional direction than the box in the first association step. This is done to ensure that the jet meanders affect the upper-level vorticity anomaly and to increase the statistical significance of the results.

To examine the correlation between the surface storm intensity and the wave amplitude, we calculate the intensity of each 300-hPa geopotential height ridge and trough. For every geopotential height isopleth peak (central peak), high or low, we take the meridional ($\Delta\theta$) and zonal ($\Delta\lambda$) distances to each of the two adjacent low or high peaks. The neighboring peak with a smaller $\Delta\theta$ is used to determine the intensity of the main peak. The intensity of the meander h is the ratio between the meridional and zonal distances between the central peak and its adjacent peak $h = \Delta\theta/\Delta\lambda$. An illustration of assessing the meridional and zonal distances of isopleth peaks can be seen in Fig. A1 in the appendix. In the two-step association process, we only consider meanders more intense than $h = 1$. The ridges and troughs are classified into five intensity levels using percentiles, with each level representing a 20th percentile range, where the most intense meander in the simulation corresponds to the 100th percentile.

This method captures Rossby waves breaking since the extrema in the geopotential height isopleths can still be detected (Thorncroft et al. 1993; Ndarana and Waugh 2010). However, the intensity of ridges and troughs during Rossby wave breaking may be underestimated depending on the wave's shape. Additionally, for cutoffs and blocking events, where geopotential height isopleths do not span all longitudes, the association algorithm will not detect them as troughs or ridges or associate them with surface storms, unless the storm reaches maximum intensity within 48 h of the cutoff or blocking event. These events can be viewed as the evolution of a trough or ridge in the 300-hPa geopotential height isopleth. This issue highlights the advantage of using an idealized GCM. The analysis can be applied to a large dataset of storms and jet meanders, ensuring that the small number of cases where Rossby wave breaking, cutoffs, or blocking events lead to underestimated wave amplitude (or no association at all) has minimal impact on the results. Here, we analyze about 20 000 surface cyclones and 20 000 surface anticyclones from 4000 simulation days. Furthermore, a dataset of only a few thousand storms would increase the statistical influence of false negatives and, more critically, false positives, cases where storms are incorrectly associated with jet meanders. To assess the algorithm's reliability, we exploit its occasional association of upper-level

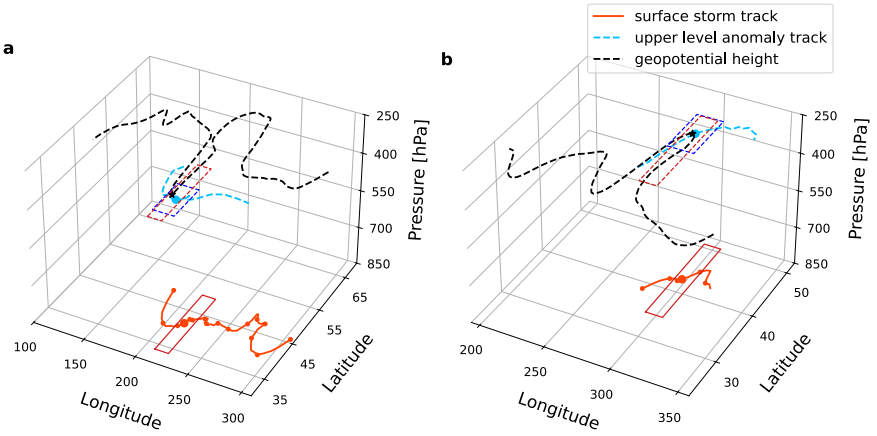

FIG. 1. Demonstration of the two-step process for associating surface (a) cyclone and (b) anticyclone with an upper-level geopotential height meander in the reference simulation. Red lines are surface storm tracks at 850 hPa, red circles are the locations of the storms every 6h, and the large circles are the locations at the time of the storm's maximum intensity t_{max}. The projection of the continuous red box on the 300-hPa pressure level, shifted five longitudes to the west, is the dashed red box. The dashed blue line is the track of the 300-hPa (a) cyclonic and (b) anticyclonic motion identified by the algorithm and located within the dashed red box at t_{max}. The dashed blue box is centered around the blue circle, the location of the upper-level vorticity anomaly at t_{max}, and in which we looked for (a) trough and (b) ridge in the 300-hPa geopotential height (black contour). The upper blue (red) box in this example is centered around (a) longitude 215° (212°) and latitude 39° (41°) and (b) longitude 295° (293°) and latitude 46° (42°).

troughs (ridges) with negative (positive) vorticity anomalies, which are dynamically inconsistent and thus serve as proxies for false associations. Comparing these to the frequency of dynamically consistent associations helps validate that the algorithm identifies surface storms that dynamically interact with jet meanders.

b. *Idealized GCM global warming simulation setup*

To investigate how global warming will affect jet meandering and storm intensity, we conduct global warming simulations by increasing the optical depth thicknesses at the equator and the pole (e.g., O'Gorman and Schneider 2008; Levine and Schneider 2011; Pfahl et al. 2015; Tamarin and Kaspi 2017b). Multiplication of both optical depth parameters by the same factor $\alpha = 1.2, 1.5, 1.8$ increases τ according to Eq. (1), hence raising the global-mean surface temperature by roughly 3, 6, and 9 K, respectively, and decreasing the equator-to-pole surface temperature difference. For $\alpha = 1$, the reference simulation, the surface temperature distribution is similar to Earth's, with around 40-K mean surface equator-to-pole difference. We apply the storm-tracking algorithm and the two-step association process to each experiment.

As part of the global atmospheric circulation, the average intensity of the meanders associated with surface storms is controlled by the mean meandering of the eddy-driven jet. We are assessing whether there was an increase in jet meandering due to global warming using the "SeaMaxMin" and "DayMaxMin" metrics described in Barnes (2013). These metrics measure the meridional extent of the 500-hPa geopotential height isopleths (Z500) on a global scale, whereas the metric introduced in section 2a, and applied in section 3c, measures the regional meridional extent of the 300-hPa geopotential height isopleths. The SeaMaxMin metric, similar to that proposed by Francis and Vavrus (2012), calculates the difference between the maximum and minimum latitudes obtained by individual Z500 isopleth at each longitude at each season. Specifically, for each season, at each longitude, it identifies the maximum and minimum latitude a specific Z500 isopleth reaches over that season, with their difference representing the isopleth's meridional extent. These extents are then zonally averaged to obtain a single value for each isopleth in each season. Since there are no seasonal variations in the model, the analysis period for SeaMaxMin only needs to exceed the typical time scale of a long-lived storm. For simplicity, we define a "season" as the models' 50-day period. It is sufficiently long to capture jet meanders and much longer than the synoptic time-scale or model-scale variability. Moreover, since we average the isopleths' extents over all the 50-day periods, any differences from using different time periods would be averaged out, making the choice of duration inconsequential. The DayMaxMin metric calculates the daily meanders of the Z500 field. For each day, it takes the difference between the maximum and minimum latitudes obtained by a single Z500 isopleth (see Fig. 1 in Barnes 2013). In contrast to Barnes (2013), who applied both metrics over a specific region, we are applying them globally. An isopleth must simultaneously contain valid values at all longitudes to be included in the analysis. We excluded missing values from the averaging process. The use of an idealized model allows us to overcome the limitations of long-term observational data, which have posed challenges in

previous studies (e.g., Francis and Vavrus 2012; Barnes 2013; Screen and Simmonds 2014). This approach enables us to determine whether the observed results stem from internal variability or from the change in the system's physical parameters.

3. Results

a. Increase in the eddy-driven jet meandering

We start by examining the relation between global warming and jet stream meandering. We conduct a series of simulations of a global increase in mean surface temperature, which results in changes to the mean surface temperature gradient and weakens the zonal wind speed in the midlatitudes, as can be seen in Fig. A2. By applying the SeaMaxMin and DayMaxMin metrics (Barnes 2013) on the idealized GCM global warming simulations, we observe an increase in jet meandering with higher mean surface temperature (Fig. 2). In Fig. 2, similar to Fig. 3 in Barnes (2013), we show the extent of the Z500 isopleths. The dashed lines represent the average Z500 isopleth identified with the eddy-driven jet in each simulation. The intersection between the solid and dashed lines of the same simulation is marked by a dot (matched colors), indicating the simulation's averaged jet meander extent. The rise in the dashed lines' height reflects the expansion of the atmospheric column due to lower-tropospheric warming (e.g., Seidel and Randel 2006). Both metrics show a correlation between higher mean surface temperatures and increased jet meandering extent.

b. Examining the relation between global warming and jet meandering

AA leads to a reduction in the Z500 meridional gradient $\partial Z/\partial y$. In addition, it weakens the zonal-mean zonal winds at 500 hPa. To analyze the eddy-driven jet meandering, we consider the zonal u and meridional v wind components and denote eddy anomalies from the time-mean values by prime. The jet at this level is located around the latitude of maximum in the eddy momentum flux convergence $-(\partial/\partial y)(u'v')$, along with the location of the maximum magnitude in the horizontal eddy streamfunction at 500 hPa, defined as $\psi' = \int v' dx$. The leading order of small meridional changes in the streamfunction, i.e., the eddy streamfunction, around its maximum value in the midlatitudes can be expressed as

$$\psi' \propto \frac{\partial \psi}{\partial y} dy, \tag{2}$$

where dy is the meridional displacement of a Lagrangian parcel from its original latitude. For a small Rossby number and a constant Coriolis parameter, the streamfunction and geopotential height field are proportional to each other $\psi \propto Z$ (Vallis 2017). Thus,

$$\psi' \propto \frac{\partial Z}{\partial y} dy. \tag{3}$$

Since we care only for the magnitude of the jet meridional extent (dy), not whether it extends northward or southward, we can take the absolute value of Eq. (2). Writing the geopotential height term in Eq. (2) as the sum of its zonal mean and eddy component ($Z = \overline{Z} + Z'$) and taking the time mean (denoted by curly brackets $\{\cdot\}$) of Eq. (3), we get

$$\{|\psi'|\} \propto \left\{\left|\frac{\partial \overline{Z}}{\partial y}\right|\right\}\{|dy|\}, \tag{4}$$

and we can address $|dy|$ as the meridional extent of the jet meandering. Its values are determined using SeaMaxMin and DayMaxMin metrics, which provided similar extent values in the idealized GCM simulations. We assume that $\partial \overline{Z}/\partial y \gg \partial Z'/\partial y$, as the background difference dominates over the anomaly in the midlatitudes. Equation (4) connects the time-averaged meridional gradient and the eddy streamfunction through the extent of the meanders of the jet. It sheds light on the change of the jet meandering in the global warming scenarios, where both $|\psi'|, \partial \overline{Z}/\partial y$ decrease in the midlatitudes (Figs. 3a,b) as a result of the reduction in the 1000–500-hPa meridional temperature gradient (Fig. 3c). The ratio between the decrease of the two terms will determine whether the jet meandering is projected to increase in global warming scenarios and presented in Fig. 3d ($Z_y \equiv \partial Z/\partial y$). It shows the increase in the time-mean values of $\Delta(\overline{|\psi'|}/Z_y)|_i = (\overline{|\psi'|}/Z_y)|_i/(\overline{|\psi'|}/Z_y)|_{\text{reference}}$ in each simulation, where the subscript i stands for the 3–9-K rise in mean surface temperature from reference simulation. The increase means that, on average, at the latitudes of the jet's center, the Z500 gradient decreases more than the eddy streamfunction. This pattern is consistent with an increase in $\overline{|dy|}$, as described by Eq. (4). This analysis does not provide an explanation for why the Z500 meridional gradient decreases more than the eddy streamfunction in these simulations, as they are both influenced by the reduction in the meridional temperature gradient. However, it shows consistency between the reduction of $\overline{|\psi'|}$ and $|\partial \overline{Z}/\partial y|$, along with the increase in jet meandering.

c. The relation between storms and jet meanders

We implement the two-step association process to investigate and quantify the connection between jet meanders and storm intensity. We first apply only the second step, independent of the surface storm association condition defined in the first step. It associates vorticity anomalies at the upper troposphere with jet meanders in the reference simulation, with the resulting association percentages depicted in Fig. 4a. The blue (orange) line represents the probability, in percent, that an upper-level positive (negative) vorticity anomaly is associated with trough (ridge) in the 300-hPa geopotential height isopleth. It shows the probability that a vorticity anomaly is associated with a jet meander for each normalized anomaly intensity, for example, slightly below 45% (above 95%) for the weakest (strongest) positive vorticity anomaly. The percentages of associated positive vorticity anomalies monotonically increase for stronger anomalies. The percentages for weak anomalies are lower, as jet meanders do not necessarily induce the vorticity anomalies, which result from other local dynamical

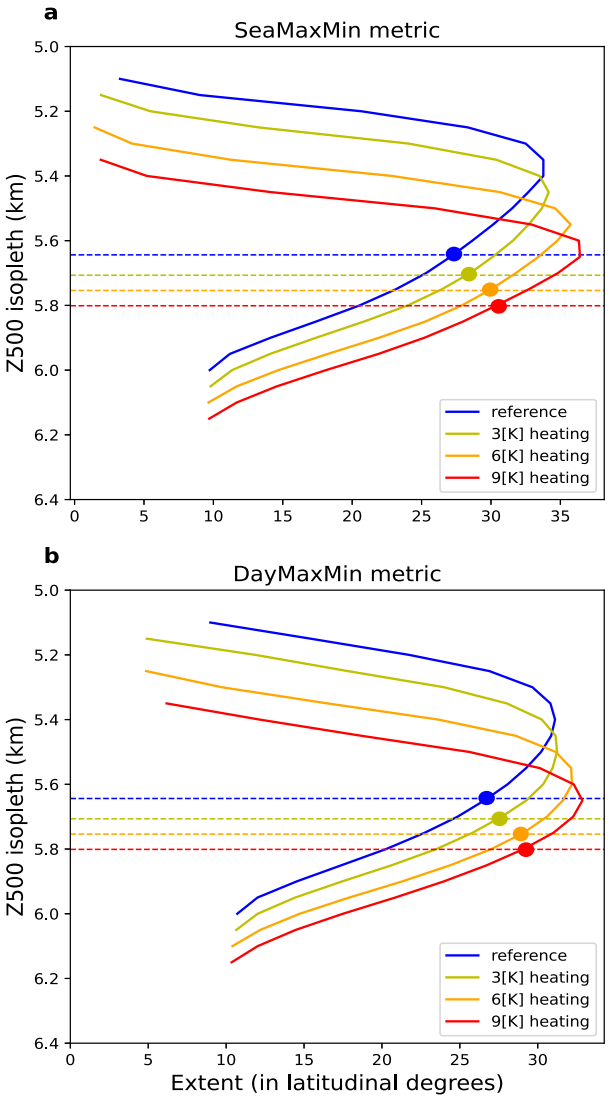

FIG. 2. The extent of 500-hPa geopotential height isopleths in idealized GCM warming simulations, calculated using (a) SeaMaxMin and (b) DayMaxMin metric. Solid lines with warmer colors indicate a higher global mean surface temperature, and the matching color dashed line represents the averaged Z500 isopleth identified with the eddy-driven jet in the simulation. The dots mark the intersection between solid and dashed lines of the same simulation. Note the inverted values in the *y* axis. The lines exhibit similar behavior to that observed in reanalysis data, as presented in Fig. 3 in Barnes (2013).

processes. The high percentages for intense anomalies indicate a strong connection between the jet meanders and the formation of upper-level cyclonic and anticyclonic vorticity anomalies, as can be expected. As anticyclones have more extensive spatial coverage than cyclones, the decrease in percentages might result from a larger distance between the center of the tracked anticyclonic motion and the peak of the meander. The overall increase in percentages for larger vorticity anomalies suggests that the shape of the eddy-driven jet governs the creation of large upper-level vorticity anomalies. The percentages of association between anticyclonic motion and a trough, or cyclonic motion and a ridge, are consistently below 10% for all vorticity anomaly intensities, indicating that these associations are more random than physically correlated.

Adding the first step that associates surface storms with upper-level vorticity anomaly, we can quantify the relation between surface cyclones and anticyclones to jet meanders. As ridges and troughs do not always align with the tracks of the upper-level vorticity anomalies they induce or influence, we consider the differences in the association times between the first and second steps. Figure 4b shows the percentages of surface storms associated with 300-hPa geopotential height meanders as a function of the time difference between the time the surface storm reaches its maximum intensity and the time the 300-hPa vorticity anomalies are associated with the meanders. The highest number of intensity level 5 storms associated with meanders is 24 (12) hours before the cyclones (anticyclones) reach their maximum intensity. The fact that this association occurs before most intensity level 5 cyclones reach their maximum intensity suggests that upper-level anomalies contribute to surface cyclone intensification. The existence of the upper-level vorticity anomaly can lead to an amplification of the lower-level vorticity anomaly. The longer time lag for cyclones stems from their baroclinic growth. The more intense the cyclone is, the longer the time lag between the interaction of the upper-level vorticity anomaly with the jet meander and the cyclone's maximum intensity. Hence, we take into account the time-lag effect in each surface storm association process. We investigate the association between ridges and troughs and upper-level vorticity anomalies within 48 h before the surface storm reaches its maximum intensity.

For the reference simulation, the percentages of the surface storms associated with jet meander as a function of the meander intensities, classified into five storm intensities, are presented in Fig. 5. Each set of colored dots, connected by a dashed line, represents a different intensity level of storms. The percentages are from the total storms in each intensity level (represented by the color), as a function of the associated meander intensity. Among intensity level 5 cyclones that are associated with any upper-level trough, the majority are linked to deep troughs, jet meanders in intensity levels 4 and 5, accounting for 30% of all intensity level 5 cyclones. In contrast, fewer than 7% are associated with weaker meanders (intensity levels 1–3). These relations also represent cyclones in intensity levels 3–4 and anticyclones in intensity levels 3–5 associated with ridges. Moreover, the sum of the percentages of each storm intensity level grows as the intensity of the storms gets higher, similar to the results of the analysis made only on the 300-hPa vorticity anomalies (Fig. 4). The percentages for weak storms are low as most of the vorticity anomalies are not significant enough to interact with the upper atmosphere. The more intense storms interact with the upper atmosphere and relate to the upper-level vorticity; hence, the association percentages for intense storms are high. Higher meander intensity linked to stronger storms indicates that the likelihood of a storm becoming stronger depends on the jet meander intensity. It is not that every intense jet meander will lead to a surface storm at some intensity level. But if a surface vorticity

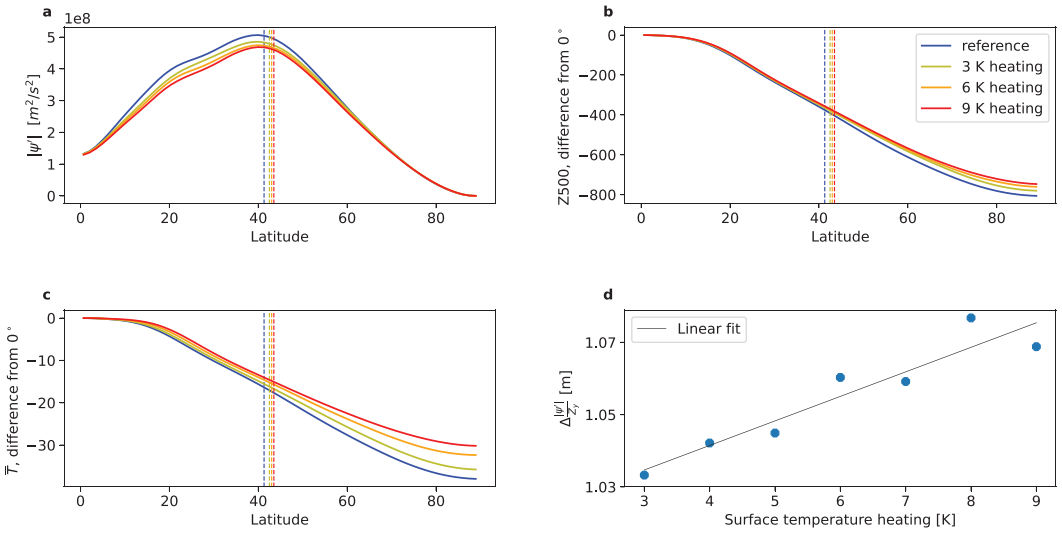

FIG. 3. Solid lines show the time and zonally averaged values of the NH (a) absolute eddy streamfunction at 500 hPa, (b) differences in 500-hPa geopotential height from the equator, and (c) differences in the 1000–500-hPa column-averaged temperature ($\overline{T}$) from the equator. Dashed vertical lines show the averaged latitude of the eddy-driven jet center. (d) The change in the ratio between the time-averaged absolute value of the eddy streamfunction and the Z500 meridional gradient for each global warming simulation. The values of $|\psi'|/Z_y$ are calculated in simulations with a 3–9-K mean temperature increase, in latitudes around the center of the jet, in comparison to the same latitudes at the reference simulation.

anomaly has been initiated and interacts with a prominent upper-atmospheric trough/ridge through an upper-level vorticity anomaly, the intensity of the trough/ridge will most likely influence the storm to become an intense surface storm. The area where the association process links a lower-level vorticity anomaly with an upper-level vorticity anomaly is based on the average size of an extratropical storm. While increasing the area size would increase association percentages, it may also introduce false associations with storms that do not dynamically interact with upper-level vorticity anomalies. This relatively small area, combined with the condition that the upper-level and lower-level anomalies will propagate in the same direction for 24 h, enhances the likelihood of correctly identifying interactions between surface storms and their associated jet meanders.

To better understand the vertical structure of the surface storms associated with jet meanders, we created composite plots for associated storms with meanders at intensity levels 1, 3, and 5 (Fig. 6). The contours are the 300-hPa geopotential height isopleths, and magenta circles show the location of the associated 300-hPa vorticity anomaly with the surface storm at the time of the surface storm's maximum intensity. Shading is surface pressure anomalies, and yellow crosses are the locations of the most significant negative (positive) surface pressure anomalies for cyclones (anticyclones). In all panels, the magenta circles are westward shifted from the location of the yellow crosses, as expected from baroclinic storms. In addition, due to the meridional advection of surface temperatures, the locations of the low (high) surface pressure anomalies are northward (southward) shifted from the upper-level vorticity anomaly. The high correlation between the shape of the geopotential height contours and the direction of the wind (arrows) in all panels implies that the flow is mainly geostrophic and follows thermal wind balance. As the geopotential height contours are more steep (more intense meander), the surface pressure anomaly (darker shading) is more significant. That is the implication of the different percentage distributions between the colors in Fig. 5. For instance, when comparing the percentages of the cyclones associated with meanders in intensity levels 3 and 5, cyclones in intensity level 5 have a larger fraction of all the cyclones associated with meanders in intensity level 5 than intensity level 3. Therefore, we observe more significant pressure anomalies in Fig. 6c than in Fig. 6b. This figure confirms that the storms analyzed exhibit a vertically baroclinic structure. Additionally, we can consider the most intense 50% of storms at intensity level 5 as extreme cyclones and anticyclones, representing 10% of all identified storms. We also applied the association analysis to the simulation with a 6-K increase in global mean surface temperature. The results, presented in Figs. A3–A5, are consistent with those of the reference simulation in Figs. 4–6, respectively. Comparing the association percentages in the reference simulation (Fig. 5) to the 6-K warming simulation (Fig. A4), we observe a slight decrease in the percentages of intensity level 5 storms (cyclones and anticyclones) associated with intensity level 5 meanders. Conversely, the percentages of intensity level 4 cyclones associated with intensity level 5 troughs show a slight increase. These results reinforce that the relations identified in the reference simulation persist under global warming simulations.

We further examine the baroclinic life cycle of the associated extratropical cyclones to strengthen the understanding of the coupling between the upper and lower pressure levels. We

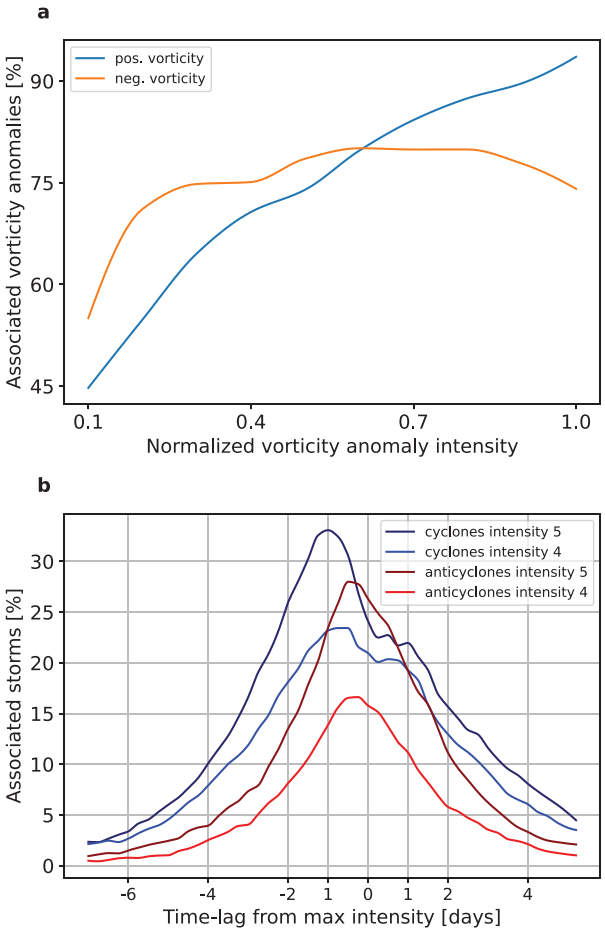

FIG. 4. (a) Association percentages between 300-hPa pressure-level positive (negative) vorticity anomalies and jet troughs (ridges) in blue (orange) as a function of the normalized vorticity anomaly intensity, at the time of the anomalies' maximum intensity. (b) Percentages of the associated intensity levels 4 and 5 surface cyclones (blue colors) and anticyclones (red colors) with 300-hPa geopotential height troughs and ridges as a function of the association time, relative to the surface storm's maximum intensity. Blue and dark blue lines indicate cyclones of intensity levels 4 and 5, respectively; red and dark red lines indicate anticyclones of intensity levels 4 and 5, respectively.

calculated the Eady growth rate (EGR) and the meridional components of baroclinic (BC_y) and barotropic (BT_y) energy conversion rates for cyclones associated with intensity level 5 troughs. These quantities are computed and averaged over all identified cyclones, with the averaging denoted by angle brackets $\langle\cdot\rangle$, and defined as $\sigma_{\mathrm{Eady}} = 0.31(f/N)\langle|\partial u/\partial z|\rangle$, $BC_y = -[\rho g^2/(N\overline{T})^2]\langle v'T'\rangle(\partial\overline{T}/\partial y)$, and $BT_y \approx -\rho\langle u'v'\rangle(\partial\overline{u}/\partial y)$ (Vallis 2006; Hadas and Kaspi 2025), where T is the temperature, N is the Brunt–Väisälä frequency, f is the Coriolis parameter, ρ is the density, and g is the gravitational acceleration. Figure 7 presents the composite evolution of the EGR, BC_y, and BT_y. Both EGR and BC_y increase around the location of the upper-level positive vorticity anomaly during the growing stage of the cyclone, peaking at the time of maximum storm intensity and subsequently declining. The BT_y peaks at the time of maximum intensity but remains approximately an order of magnitude smaller than the baroclinic conversion. This behavior aligns with baroclinic instability dynamics, which involve vertical coupling between the 300- and 850-hPa pressure levels.

The distributions of storm intensities at their peak vorticity anomaly in the global warming simulations are shown in Fig. 8. As the mean surface temperature rises, more intense upper-level (larger than $|7 \times 10^{-5}|$ s^{-1}) cyclonic and anticyclonic vorticity anomalies have been identified. In addition, the total number of identified upper-level cyclonic and anticyclonic motions increases. The strong relation between the meander intensity and upper-level relative vorticity values, shown in Fig. 4, can potentially explain the increase in the number of identified upper-level vorticity values and, in particular, the number of intense vorticity cases. As the jet amplitude increases with the mean surface temperature rise, it advects colder (warmer) temperatures toward the equator (pole), generating larger positive (negative) relative vorticity values. The upper-level vorticity, in turn, can reinforce lower-tropospheric vorticity anomalies, developing into lower-level storms. Continuing to the distributions of the lower-level storms, the total number of cyclones and anticyclones has slightly decreased

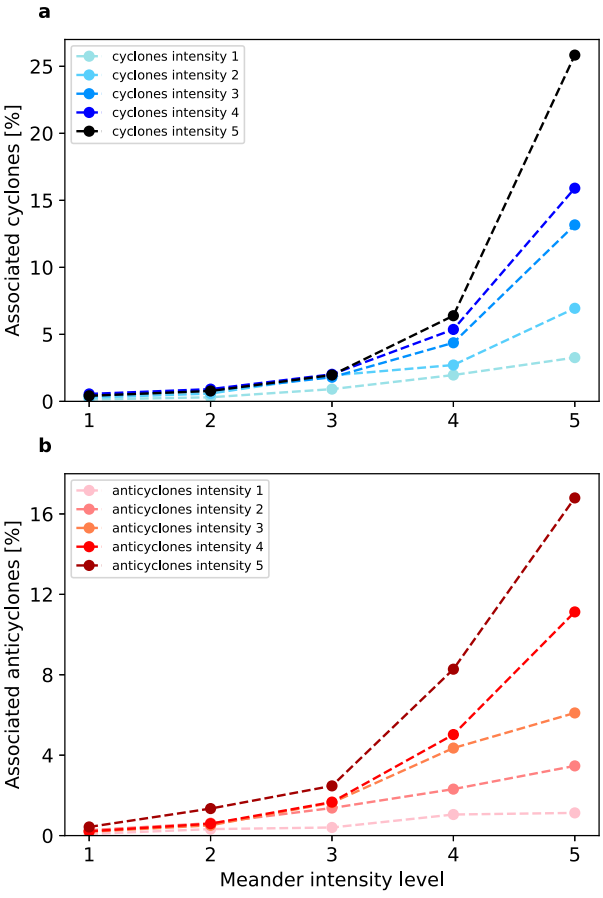

FIG. 5. Percentages of the associated surface (a) cyclones and (b) anticyclones in different storm intensity levels as a function of the jet meander intensity in the reference simulation. Colors represent the intensity level of the surface storm.

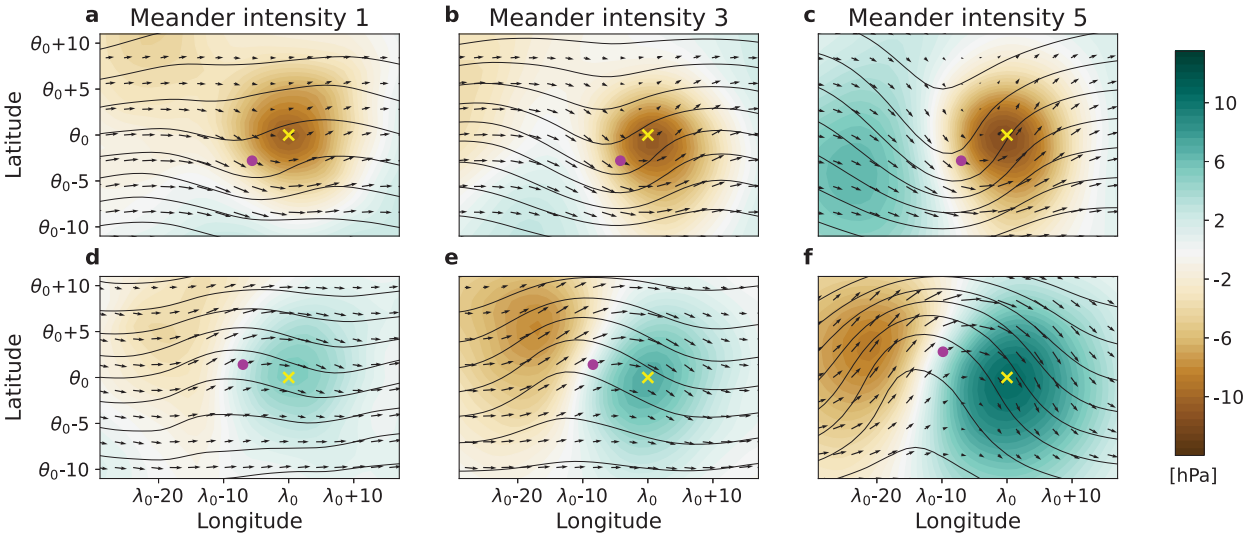

FIG. 6. Composite plots of the lower-level (top) cyclone and (bottom) anticyclone associated with a meander in intensity levels 1, 3, and 5 in the reference simulation. Shading is the surface pressure anomalies, yellow cross represents the location of the most significant anomaly (longitude λ_0, latitude θ_0), and black contours and arrows are 300-hPa geopotential height and wind velocity, respectively. The magenta circle shows the location of the associated upper-level vorticity anomaly center.

with the increase in mean temperature. For intensity level 5 storms, cyclones (anticyclones) with maximum relative vorticity exceeding the 80th percentile dashed line in Figs. 8c and 8d exhibit a shift toward higher values as the mean surface temperature increases. Intensity level 5 cyclones show a larger shift to higher values compared to intensity level 5 anticyclones. That makes the last connection between global warming and storm intensification. Using idealized GCM global warming simulations, we tied between mean surface temperature rise, particularly AA, through an increase in the eddy-driven jet meandering and an increase in lower-level storm intensities, potentially leading to storm intensification.

4. Conclusions

The connection between global warming and the intensification of storms has been studied extensively but has led to a

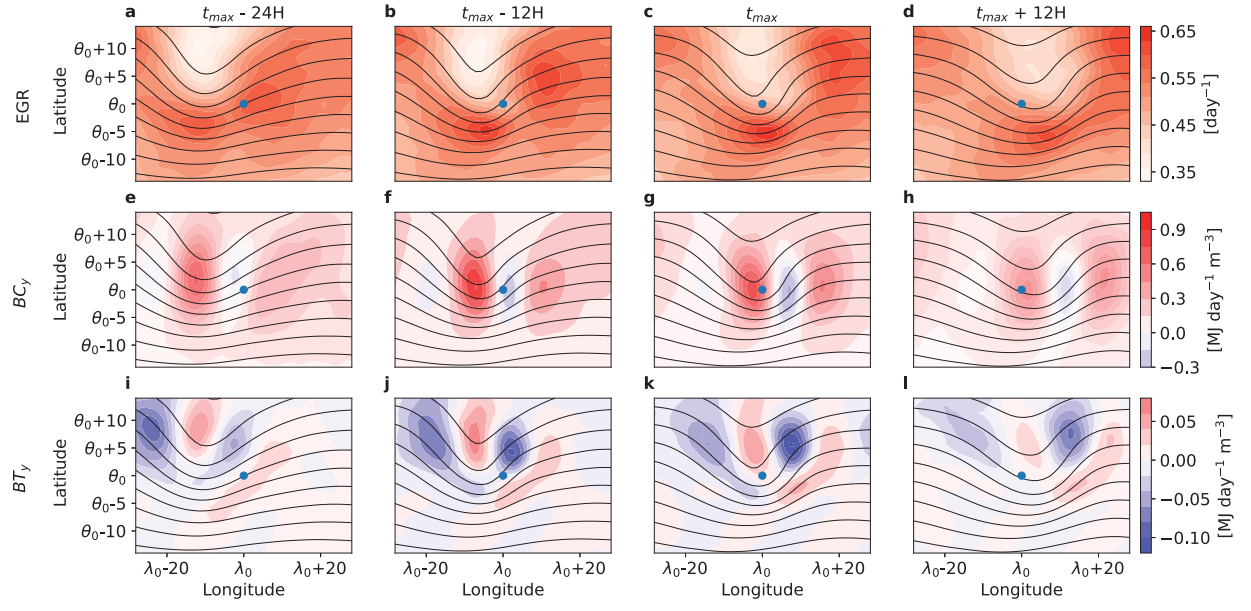

FIG. 7. Shadings are (a)–(d) EGR, (e)–(h) meridional component of the baroclinic conversion rate, and (i)–(l) meridional component of the barotropic conversion rate, at −24, −12, 0, and + 12 h relative to surface cyclone maximum intensity time. Contours are 300-hPa geopotential height isopleths. Blue circles are the identified 300-hPa positive vorticity anomaly. Values are averaged over surface cyclones associated with intensity level 5 troughs.

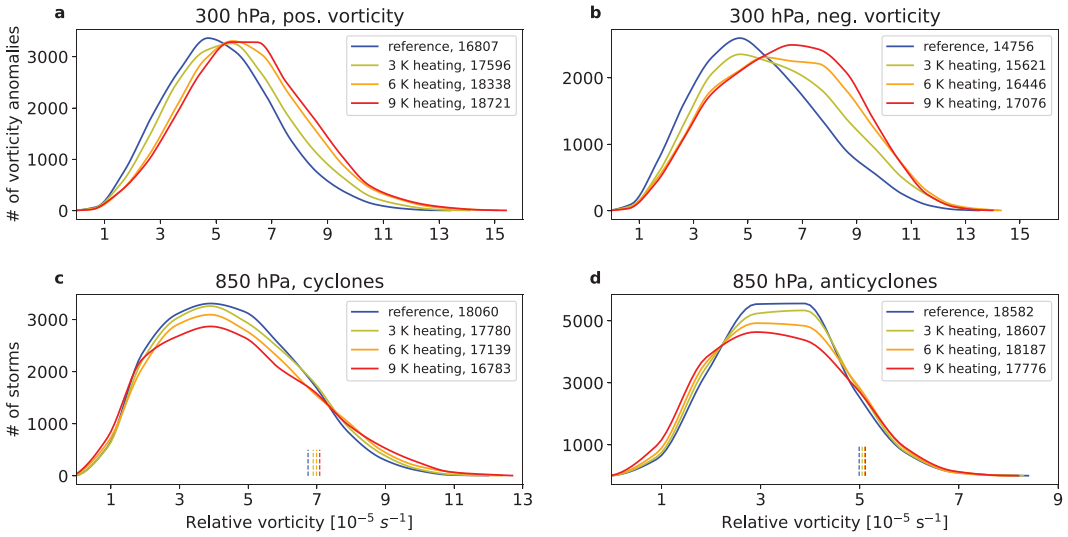

FIG. 8. Storm intensity distributions for the idealized GCM simulations. (a),(b) The distributions of the upper-level (300 hPa) relative vorticity values. (c),(d) Distributions of lower-level (850 hPa) relative vorticity values. Warmer color represents simulation with higher global-mean surface temperature. The total number of 300- and 850-hPa-analyzed vorticity appears in the legend of each simulation. Dashed vertical lines indicate the 80th percentile of vorticity anomalies for each simulation, with matching colors, for 850-hPa cyclones in (c) and anticyclones in (d).

wide range of results. Here, using an idealized aquaplanet GCM, we systematically quantify the percentages of storms associated with jet meanders and the correlation between larger jet meanders and storm intensity. In agreement with the hypothesis of Francis and Vavrus (2012), we show a positive correlation between the meridional gradient of midtroposphere temperatures and eddy-driven jet speed in the idealized GCM global warming simulations. The decrease in jet speed is driven by a weakened meridional temperature gradient in the 1000–500-hPa pressure layer, primarily due to AA, resulting in reduced eddy momentum flux convergence in the midlatitudes.

Using an idealized moist aquaplanet GCM provides several key advantages, including the ability to generate a large dataset of storms and jet meanders, and a simplified framework that facilitates a clearer analysis of the physical parameters affecting jet meandering. Previous studies have used numerical simulations and idealized GCMs to address the link between jet meandering and extreme weather events (e.g., Hassanzadeh et al. 2014; Moon et al. 2022; De Luca et al. 2024). However, they have not systematically examined and quantified the relation between jet meanders and storm intensity. Alongside the advantages of using an idealized model, important differences exist between this model and more complex climate models, such as those in the Coupled Model Intercomparison Project phase 6 (CMIP6). The idealized GCM has no topography; hence, it lacks stationary Rossby waves. Additionally, as the radiation does not feedback with water vapor, clouds, and sea ice, the warming is a uniform scaling of the gray optical depth [Eq. (1)] without spatial dependence in the above feedbacks. Despite these differences, this study focuses on the fundamental relations between jet meandering and storm intensity, which is primarily influenced by transient waves rather than stationary wave features (e.g., Kaspi and Schneider 2013; Screen and Simmonds 2014; Kornhuber et al. 2020). While land–sea contrasts play a prominent role in shaping regional climate responses, the underlying dynamical mechanisms investigated here are expected to be relevant in more complex settings. Moreover, the uniform forcing provides a controlled framework to isolate the effects of a reduced meridional temperature gradient on jet dynamics and storm intensity, independent of additional radiative feedbacks.

To assess the changes in jet meandering in global warming simulations, we use SeaMaxMin and DayMaxMin metrics presented by Barnes (2013). We observe an increase in the jet meridional extent in both metrics with global warming (Fig. 2). To further explore jet meandering changes and the link with its zonal velocity, we demonstrate a direct correlation between the eddy streamfunction and the product of the Z500 meridional gradient and the jet's meridional extent [Eq. (4)]. The time-averaged ratio of the absolute eddy streamfunction at the jet center to the Z500 meridional gradient around it increases in global warming simulations, coinciding with enhanced jet meandering. Figure 3 shows an increase in $\{|\overline{\psi'}|/Z_y\}$ across simulations, consistent with the rise in jet meandering ($\{|dy|\}$) observed in Fig. 2.

The Lagrangian perspective adopted in this study allows us to track jet meanders, upper-level vorticity anomalies, and storm development, providing insights into their causal link. We develop a method for associating jet meanders with storm development, that considers the location of the storm's center relative to the ridge or trough and the meridional extent of the meander. The percentages of a strong surface storm (cyclone or anticyclone) associated with a Z500 isopleth meanders

grow as the storms' intensity increases. Moreover, large Z500 isopleth meanders are mainly associated with intense cyclones and anticyclones, pointing to a strong link between the extent of the jet meander and the storm's intensity (Fig. 5). We deduce that increased jet meandering leads to more significant upper-level vorticity anomalies that induce stronger storms. This link is highlighted by the results shown in Fig. 4b. A time lag between the time an upper-level trough or ridge becomes associated with lower-level vorticity anomaly and the time the storm reaches its maximum intensity (i.e., maximum vorticity anomaly) is seen in most of the associated storms. The interaction between upper-level and lower-level vorticity anomalies is mutually reinforcing. At the same time, the fact that this association occurs before most intensity level 5 cyclones reach their maximum intensity suggests that upper-level anomalies play a role in intensifying cyclones. The relation between strong jet meanders and strong storms implies that stronger jet meanders will reinforce lower-level vorticity anomalies to develop into more intense storms. Storm intensity distributions of the global warming simulations present an increase in cyclone and anticyclone intensities (Fig. 8). For each 1-K rise in the mean surface temperature, there is an average increase of 0.6% in the 80th percentile of the storm intensity distribution.

Our idealized aquaplanet GCM warming simulations indicate that AA reduces lower-tropospheric baroclinicity in the midlatitudes, leading to a decrease in the eddy-driven jet speed and weakening the storm tracks. This response resembles observed and projected changes in NH summer under climate change (e.g., Coumou et al. 2015; Kang et al. 2023). While previous studies have suggested that a faster eddy-driven jet is associated with more intense storms (e.g., Lukens et al. 2018), our simulations show an increase in storm intensity despite a reduction in zonal wind speed. This finding suggests that a weakened storm track, often linked to reduced eddy kinetic energy (EKE), might not necessarily imply weaker storms. A possible explanation for this distinction is that the integrated effect of many eddies shapes storm tracks, whereas storm intensity is determined by localized energy conversions (Chang and Guo 2012). If AA weakens the baroclinic zone, the overall storm-track activity may weaken. However, individual storms may still intensify if diabatic heating or significant localized pressure gradients lead to stronger energy conversion. Notably, previous studies using more complex future climate models have projected a slight decrease in NH summer storm intensity, in contrast to our findings (e.g., Chang et al. 2016; Priestley and Catto 2022). This study does not attempt to directly compare the magnitude of AA or storm-track weakening with previous studies, as the idealized model is not designed to reproduce observed climatology but rather to isolate physical mechanisms and capture key dynamical features of the general circulation. Nonetheless, the trends identified in the idealized model align closely with observed patterns of NH summer circulation, supporting the relevance of our findings despite the simplified model framework. Future work using more complex setting, including a detailed assessment of the association between surface storms and upper-level jet meanders, may help resolve these discrepancies.

In this study, we investigate the link between eddy-driven jet meanders and extratropical storm intensity in an idealized framework. Our results reveal a strong correlation, with intense storms more likely associated with intense jet meanders than weak ones. Additionally, the time-lag analysis suggests that intense upper-level jet meanders can contribute to the baroclinic amplification of surface storms. Under global warming conditions, both jet meandering and storm intensity increase, highlighting a potential link between amplified upper-level Rossby waves and stronger storms in a warming climate.

Acknowledgments. This research has been supported by the Israeli Science Foundation (Grant 996/20). We thank Or Hadas and Ilai Guendelman for their suggestions and assistance in implementing the model and tracking algorithm. Computational work was carried out on the Weizmann HPC facility CHEMFARM, supported by the WIS Ben May Center for Chemical Theory and Computation.

Data availability statement. The data from the idealized GCM simulations are available upon request at eaviv8@gmail.com and yohai.kaspi@weizmann.ac.il.

APPENDIX

Illustration of Meander Intensity Metric, Reference Parameters, and 6-K Warming Figures

Figure A1 illustrates the meander intensity assessment metric. Figure A2 shows the spatial distribution of temperature, zonal wind, and EKE in the reference simulation, along with their differences in the global warming simulations. Figures A3–A5

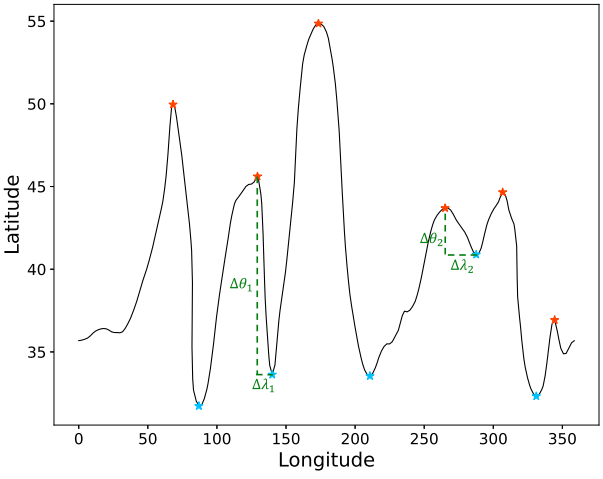

FIG. A1. Illustration of the assessment metric used to calculate the meridional ($\Delta\theta$) and zonal ($\Delta\lambda$) distances of isopleth peaks for determining meander intensity (h). The solid line is a 300-hPa geopotential height isopleth in a given instance. Red (blue) asterisks denote high (low) peaks. Dashed green vertical (horizontal) lines indicate the meridional (zonal) distances used to calculate the meander intensity. The intensity of the second high peak is given by $h_1 = \Delta\theta_1/\Delta\lambda_1$, and the fourth high peak is $h_2 = \Delta\theta_2/\Delta\lambda_2$. In this example, $h_1 > h_2$.

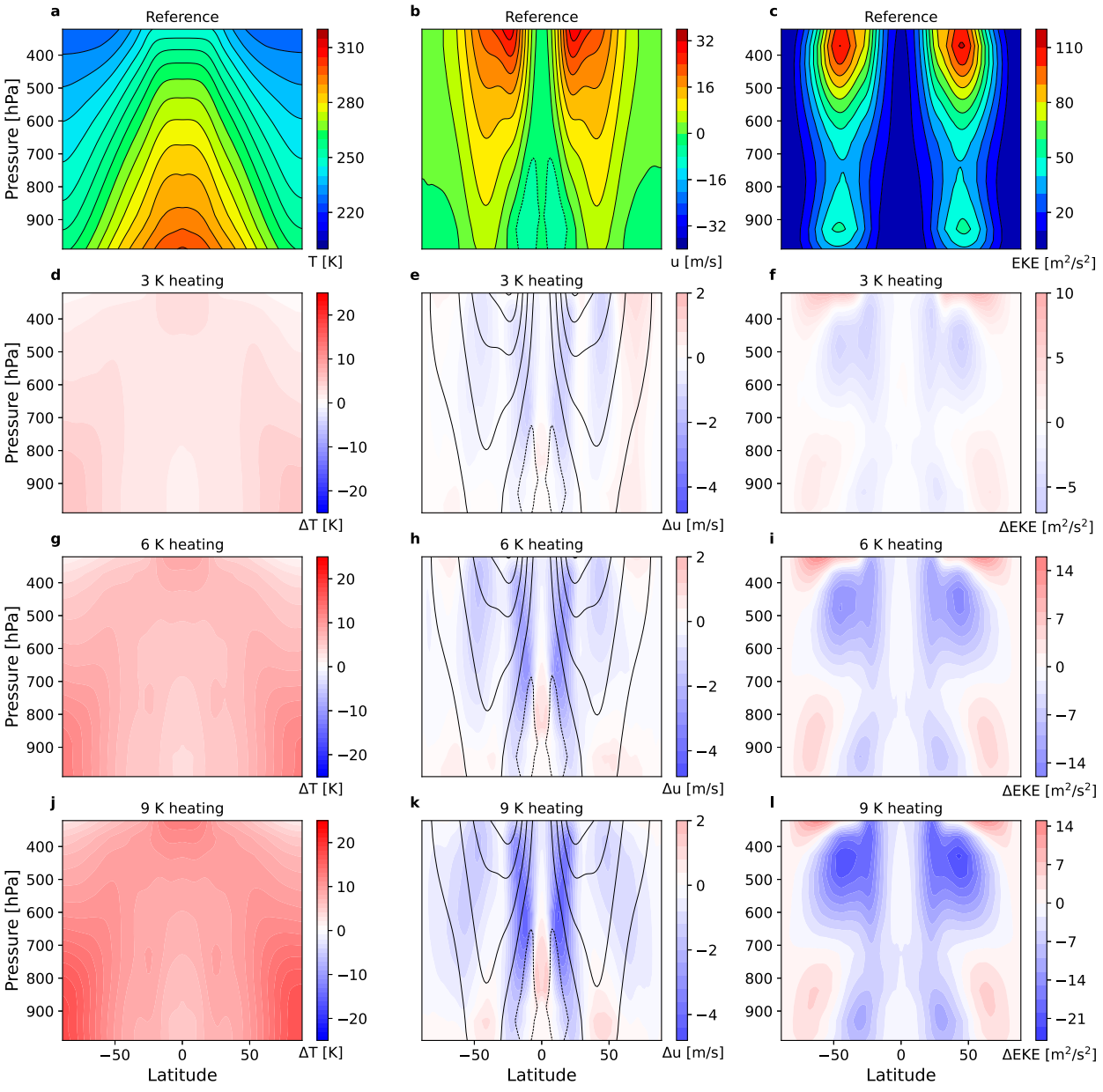

FIG. A2. Shadings are the time and zonal mean of (left) temperature, (middle) zonal wind, and (right) EKE of the idealized GCM simulations. (a)–(c) The reference simulation values. (d), (g), (j) Temperature differences. (e), (h), (k) Zonal wind differences. (f), (i), (l) EKE differences between the simulations of an increase in mean surface temperature by 3, 6, and 9 K and the reference simulation, respectively. In (a), black contours indicate the time- and zonal-mean temperature (5-K intervals). Black contours show the simulations' time and zonal mean of zonal wind, with contour intervals of 4 m s^{-1} in (b) and 7 m s^{-1} in (e), (h), and (k). In (c), black contours show the time- and zonal-mean EKE with 10 m^2 s^{-2} intervals.

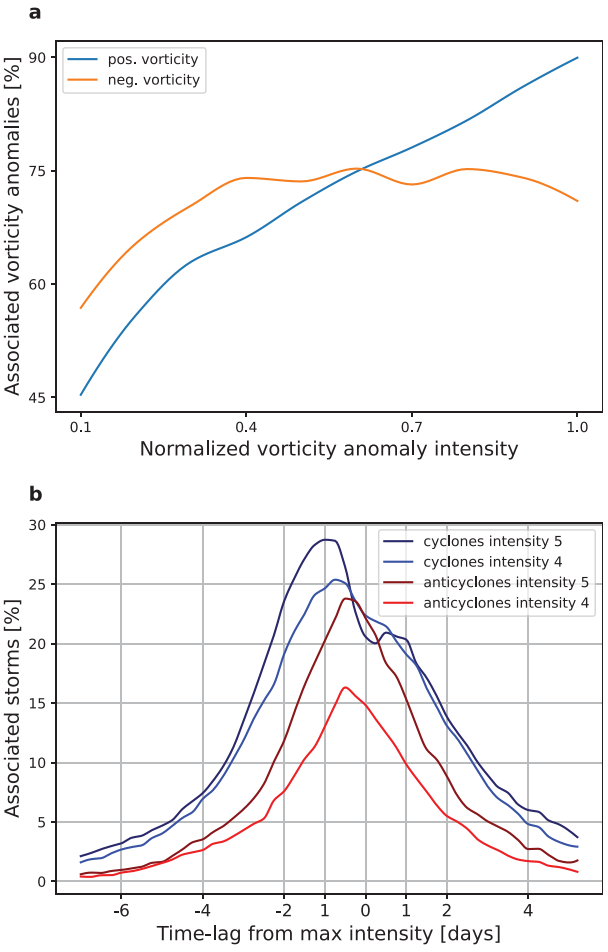

FIG. A3. As in Fig. 4, but for global warming simulation with 6-K rise in mean surface temperature.

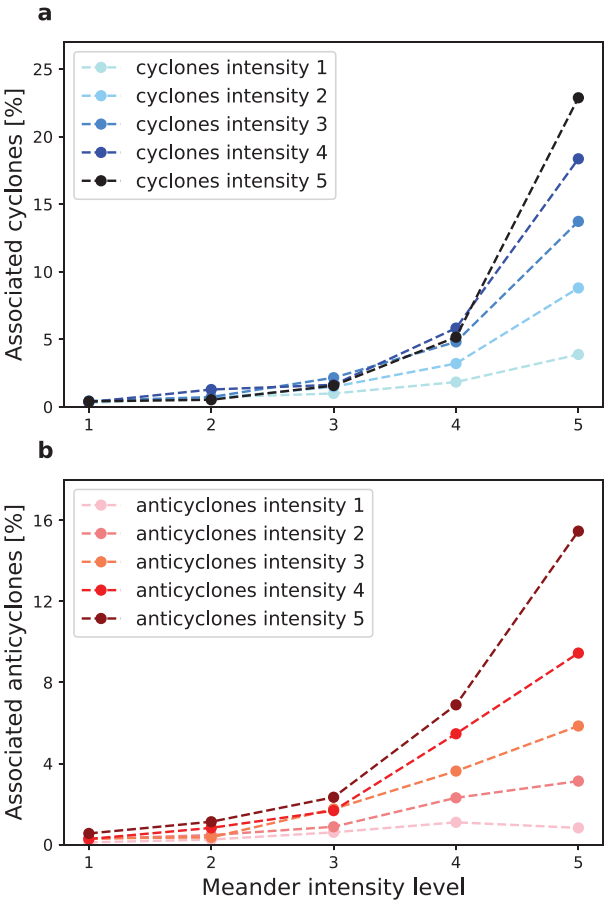

FIG. A4. As in Fig. 5, but for global warming simulation with 6-K rise in mean surface temperature.

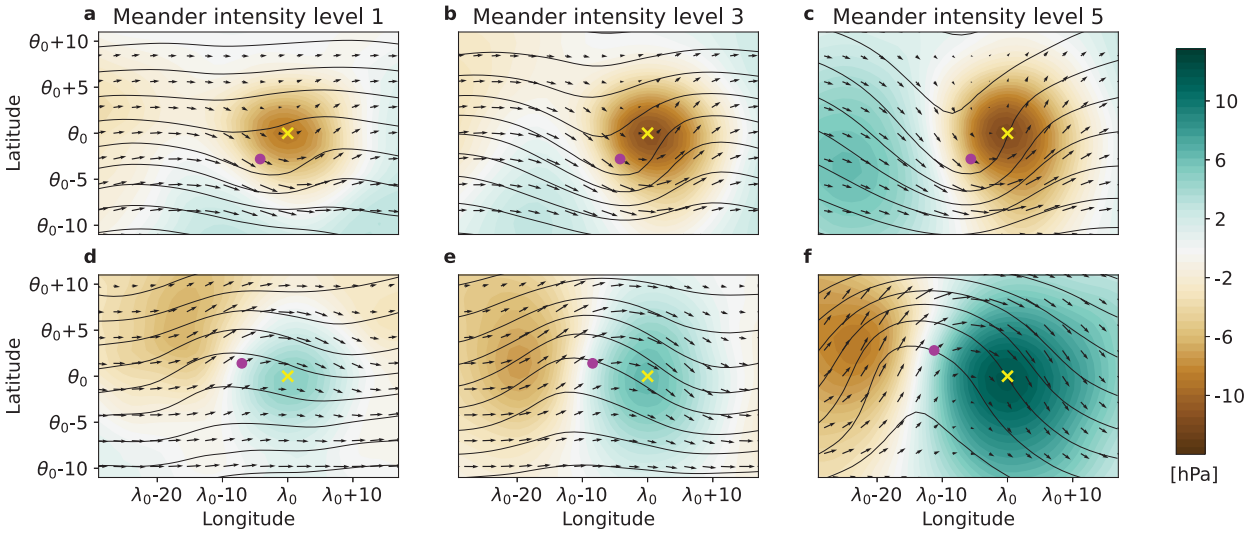

FIG. A5. As in Fig. 6, but for global warming simulation with 6-K rise in mean surface temperature.

correspond to Figs. 4–6 in the main text, but for the simulation with a 6-K increase in mean surface temperature.

REFERENCES

Afargan, H., and Y. Kaspi, 2017: A midwinter minimum in North Atlantic storm track intensity during in years of a strong jet. *Geophys. Res. Lett.*, **44**, 12 511–12 518, https://doi.org/10.1002/2017GL075136.

Anderson, J. L., and Coauthors, 2004: The new GFDL global atmosphere and land model AM2–LM2: Evaluation with prescribed SST simulations. *J. Climate*, **17**, 4641–4673, https://doi.org/10.1175/JCLI-3223.1.

Barnes, E. A., 2013: Revisiting the evidence linking Arctic amplification to extreme weather in midlatitudes. *Geophys. Res. Lett.*, **40**, 4734–4739, https://doi.org/10.1002/grl.50880.

——, and L. M. Polvani, 2015: CMIP5 projections of Arctic amplification, of the North American/North Atlantic circulation, and of their relationship. *J. Climate*, **28**, 5254–5271, https://doi.org/10.1175/JCLI-D-14-00589.1.

Blackport, R., and J. A. Screen, 2020: Weakened evidence for mid-latitude impacts of Arctic warming. *Nat. Climate Change*, **10**, 1065–1066, https://doi.org/10.1038/s41558-020-00954-y.

——, and J. C. Fyfe, 2022: Climate models fail to capture strengthening wintertime North Atlantic jet and impacts on Europe. *Sci. Adv.*, **8**, eabn3112, https://doi.org/10.1126/sciadv.abn3112.

Brunner, L., N. Schaller, J. Anstey, J. Sillmann, and A. K. Steiner, 2018: Dependence of present and future European temperature extremes on the location of atmospheric blocking. *Geophys. Res. Lett.*, **45**, 6311–6320, https://doi.org/10.1029/2018GL077837.

Butler, A. H., D. W. J. Thompson, and R. Heikes, 2010: The steady-state atmospheric circulation response to climate change–like thermal forcings in a simple general circulation model. *J. Climate*, **23**, 3474–3496, https://doi.org/10.1175/2010JCLI3228.1.

Cattiaux, J., Y. Peings, D. Saint-Martin, N. Trou-Kechout, and S. J. Vavrus, 2016: Sinuosity of midlatitude atmospheric flow in a warming world. *Geophys. Res. Lett.*, **43**, 8259–8268, https://doi.org/10.1002/2016GL070309.

Chang, E. K. M., and Y. Guo, 2012: Is Pacific storm-track activity correlated with the strength of upstream wave seeding? *J. Climate*, **25**, 5768–5776, https://doi.org/10.1175/JCLI-D-11-00555.1.

——, C.-G. Ma, C. Zheng, and A. M. W. Yau, 2016: Observed and projected decrease in Northern Hemisphere extratropical cyclone activity in summer and its impacts on maximum temperature. *Geophys. Res. Lett.*, **43**, 2200–2208, https://doi.org/10.1002/2016GL068172.

Chemke, R., and D. Coumou, 2024: Human influence on the recent weakening of storm tracks in boreal summer. *npj Climate Atmos. Sci.*, **7**, 86, https://doi.org/10.1038/s41612-024-00640-2.

Chen, G., J. Lu, D. A. Burrows, and L. R. Leung, 2015: Local finite-amplitude wave activity as an objective diagnostic of midlatitude extreme weather. *Geophys. Res. Lett.*, **42**, 10 952–10 960, https://doi.org/10.1002/2015GL066959.

——, P. Zhang, and J. Lu, 2020: Sensitivity of the latitude of the westerly jet stream to climate forcing. *Geophys. Res. Lett.*, **47**, e2019GL086563, https://doi.org/10.1029/2019GL086563.

——, Y. Nie, and Y. Zhang, 2022: Jet stream meandering in the Northern Hemisphere winter: An advection–diffusion perspective. *J. Climate*, **35**, 2055–2073, https://doi.org/10.1175/JCLI-D-21-0411.1.

Cohen, J., and Coauthors, 2020: Divergent consensuses on Arctic amplification influence on midlatitude severe winter weather. *Nat. Climate Change*, **10**, 20–29, https://doi.org/10.1038/s41558-019-0662-y.

Coumou, D., J. Lehmann, and J. Beckmann, 2015: The weakening summer circulation in the Northern Hemisphere mid-latitudes. *Science*, **348**, 324–327, https://doi.org/10.1126/science.1261768.

Dai, A., and M. Song, 2020: Little influence of Arctic amplification on mid-latitude climate. *Nat. Climate Change*, **10**, 231–237, https://doi.org/10.1038/s41558-020-0694-3.

De Luca, P., B. Jiménez-Esteve, L. Degenhardt, S. Schemm, and S. Pfahl, 2024: Enhanced blocking frequencies in very-high resolution idealized climate model simulations. *Geophys. Res. Lett.*, **51**, e2024GL111016, https://doi.org/10.1029/2024GL111016.

Di Capua, G., and D. Coumou, 2016: Changes in meandering of the Northern Hemisphere circulation. *Environ. Res. Lett.*, **11**, 094028, https://doi.org/10.1088/1748-9326/11/9/094028.

Dole, R., and Coauthors, 2011: Was there a basis for anticipating the 2010 Russian heat wave? *Geophys. Res. Lett.*, **38**, L06702, https://doi.org/10.1029/2010GL046582.

Feldl, N., and T. M. Merlis, 2021: Polar amplification in idealized climates: The role of ice, moisture, and seasons. *Geophys. Res. Lett.*, **48**, e2021GL094130, https://doi.org/10.1029/2021GL094130.

Francis, J. A., and S. J. Vavrus, 2012: Evidence linking Arctic amplification to extreme weather in mid-latitudes. *Geophys. Res. Lett.*, **39**, L06801, https://doi.org/10.1029/2012GL051000.

——, and ——, 2015: Evidence for a wavier jet stream in response to rapid Arctic warming. *Environ. Res. Lett.*, **10**, 014005, https://doi.org/10.1088/1748-9326/10/1/014005.

Frierson, D. M. W., I. M. Held, and P. Zurita-Gotor, 2006: A gray-radiation aquaplanet moist GCM. Part I: Static stability and eddy scale. *J. Atmos. Sci.*, **63**, 2548–2566, https://doi.org/10.1175/JAS3753.1.

Geen, R., S. I. Thomson, J. A. Screen, R. Blackport, N. T. Lewis, R. Mudhar, W. J. M. Seviour, and G. K. Vallis, 2023: An explanation for the metric dependence of the midlatitude jet-waviness change in response to polar warming. *Geophys. Res. Lett.*, **50**, e2023GL105132, https://doi.org/10.1029/2023GL105132.

Hadas, O., and Y. Kaspi, 2025: A Lagrangian perspective on the growth of midlatitude storms. *AGU Adv.*, **6**, e2024AV001555, https://doi.org/10.1029/2024AV001555.

Harvey, B. J., L. C. Shaffrey, and T. J. Woollings, 2014: Equator-to-pole temperature differences and the extra-tropical storm track responses of the CMIP5 climate models. *Climate Dyn.*, **43**, 1171–1182, https://doi.org/10.1007/s00382-013-1883-9.

——, P. Cook, L. C. Shaffrey, and R. Schiemann, 2020: The response of the Northern Hemisphere storm tracks and jet streams to climate change in the CMIP3, CMIP5, and CMIP6 climate models. *J. Geophys. Res.*, **125**, e2020JD032701, https://doi.org/10.1029/2020JD032701.

Hassanzadeh, P., Z. Kuang, and B. F. Farrell, 2014: Responses of midlatitude blocks and wave amplitude to changes in the meridional temperature gradient in an idealized dry GCM. *Geophys. Res. Lett.*, **41**, 5223–5232, https://doi.org/10.1002/2014GL060764.

Hodges, K. I., 1995: Feature tracking on the unit sphere. *Mon. Wea. Rev.*, **123**, 3458–3465, https://doi.org/10.1175/1520-0493(1995)123<3458:FTOTUS>2.0.CO;2.

Hoskins, B., and T. Woollings, 2015: Persistent extratropical regimes and climate extremes. *Curr. Climate Change Rep.*, **1**, 115–124, https://doi.org/10.1007/s40641-015-0020-8.

——, M. E. McIntyre, and A. W. Robertson, 1985: On the use and significance of isentropic potential vorticity maps. *Quart. J. Roy. Meteor. Soc.*, **111**, 877–946, https://doi.org/10.1002/qj.49711147002.

Jeevanjee, N., P. Hassanzadeh, S. Hill, and A. Sheshadri, 2017: A perspective on climate model hierarchies. *J. Adv. Model. Earth Syst.*, **9**, 1760–1771, https://doi.org/10.1002/2017MS001038.

Kang, J. M., T. A. Shaw, and L. Sun, 2023: Arctic sea ice loss weakens Northern Hemisphere summertime storminess but not until the late 21st century. *Geophys. Res. Lett.*, **50**, e2022GL102301, https://doi.org/10.1029/2022GL102301.

Kaspi, Y., and T. Schneider, 2013: The role of stationary eddies in shaping midlatitude storm tracks. *J. Atmos. Sci.*, **70**, 2596–2613, https://doi.org/10.1175/JAS-D-12-082.1.

——, and A. P. Showman, 2015: Atmospheric dynamics of terrestrial exoplanets over a wide range of orbital and atmospheric parameters. *Astrophys. J.*, **804**, 60, https://doi.org/10.1088/0004-637X/804/1/60.

Kornhuber, K., D. Coumou, E. Vogel, C. Lesk, J. F. Donges, J. Lehmann, and R. M. Horton, 2020: Amplified Rossby waves enhance risk of concurrent heatwaves in major breadbasket regions. *Nat. Climate Change*, **10**, 48–53, https://doi.org/10.1038/s41558-019-0637-z.

Levine, X. J., and T. Schneider, 2011: Response of the Hadley circulation to climate change in an aquaplanet GCM coupled to a simple representation of ocean heat transport. *J. Atmos. Sci.*, **68**, 769–783, https://doi.org/10.1175/2010JAS3553.1.

Lu, J., G. Chen, and D. M. W. Frierson, 2008: Response of the zonal mean atmospheric circulation to El Niño versus global warming. *J. Climate*, **21**, 5835–5851, https://doi.org/10.1175/2008JCLI2200.1.

Lukens, K. E., E. H. Berbery, and K. I. Hodges, 2018: The imprint of strong-storm tracks on winter weather in North America. *J. Climate*, **31**, 2057–2074, https://doi.org/10.1175/JCLI-D-17-0420.1.

Manabe, S., and R. J. Stouffer, 1980: Sensitivity of a global climate model to an increase of CO_2 concentration in the atmosphere. *J. Geophys. Res.*, **85**, 5529–5554, https://doi.org/10.1029/JC085iC10p05529.

Martin, J. E., 2021: Recent trends in the waviness of the Northern Hemisphere wintertime polar and subtropical jets. *J. Geophys. Res.*, **126**, e2020JD033668, https://doi.org/10.1029/2020JD033668.

Moon, W., B.-M. Kim, G.-H. Yang, and J. S. Wettlaufer, 2022: Wavier jet streams driven by zonally asymmetric surface thermal forcing. *Proc. Natl. Acad. Sci. USA*, **119**, e2200890119, https://doi.org/10.1073/pnas.2200890119.

Ndarana, T., and D. W. Waugh, 2010: The link between cut-off lows and Rossby wave breaking in the Southern Hemisphere. *Quart. J. Roy. Meteor. Soc.*, **136**, 869–885, https://doi.org/10.1002/qj.627.

Nie, Y., Y. Zhang, G. Chen, and X.-Q. Yang, 2022: Quantifying eddy generation and dissipation in the jet response to upper- versus lower-level thermal forcing. *J. Atmos. Sci.*, **79**, 2703–2720, https://doi.org/10.1175/JAS-D-21-0307.1.

——, G. Chen, J. Lu, W. Zhou, and Y. Zhang, 2023: Constraining the varied response of Northern Hemisphere winter circulation waviness to climate change. *Geophys. Res. Lett.*, **50**, e2022GL102150, https://doi.org/10.1029/2022GL102150.

O'Gorman, P. A., and T. Schneider, 2008: The hydrological cycle over a wide range of climates simulated with an idealized GCM. *J. Climate*, **21,** 3815–3832, https://doi.org/10.1175/2007JCLI2065.1.

Ossó, A., and Coauthors, 2025: Advancing our understanding of eddy-driven jet stream responses to climate change–A roadmap. *Curr. Climate Change Rep.*, **11**, 2, https://doi.org/10.1007/s40641-024-00199-3.

Overland, J. E., and Coauthors, 2021: How do intermittency and simultaneous processes obfuscate the Arctic influence on midlatitude winter extreme weather events? *Environ. Res. Lett.*, **16**, 043002, https://doi.org/10.1088/1748-9326/abdb5d.

Peings, Y., J. Cattiaux, S. J. Vavrus, and G. Magnusdottir, 2018: Projected squeezing of the wintertime North-Atlantic jet.

Environ. Res. Lett., **13**, 074016, https://doi.org/10.1088/1748-9326/aacc79.

Pfahl, S., and H. Wernli, 2012: Quantifying the relevance of atmospheric blocking for co-located temperature extremes in the Northern Hemisphere on (sub-)daily time scales. *Geophys. Res. Lett.*, **39**, L12807, https://doi.org/10.1029/2012GL052261.

——, P. A. O'Gorman, and M. S. Singh, 2015: Extratropical cyclones in idealized simulations of changed climates. *J. Climate*, **28**, 9373–9392, https://doi.org/10.1175/JCLI-D-14-00816.1.

Pithan, F., and T. Mauritsen, 2014: Arctic amplification dominated by temperature feedbacks in contemporary climate models. *Nat. Geosci.*, **7**, 181–184, https://doi.org/10.1038/ngeo2071.

Previdi, M., K. L. Smith, and L. M. Polvani, 2021: Arctic amplification of climate change: A review of underlying mechanisms. *Environ. Res. Lett.*, **16**, 093003, https://doi.org/10.1088/1748-9326/ac1c29.

Priestley, M. D. K., and J. L. Catto, 2022: Future changes in the extratropical storm tracks and cyclone intensity, wind speed, and structure. *Wea. Climate Dyn.*, **3**, 337–360, https://doi.org/10.5194/wcd-3-337-2022.

Rhines, P. B., 1975: Waves and turbulence on a beta-plane. *J. Fluid Mech.*, **69**, 417–443, https://doi.org/10.1017/S0022112075001504.

Robert, L., G. Riviére, and F. Codron, 2019: Effect of upper- and lower-level baroclinicity on the persistence of the leading mode of midlatitude jet variability. *J. Atmos. Sci.*, **76**, 155–169, https://doi.org/10.1175/JAS-D-18-0010.1.

Röthlisberger, M., S. Pfahl, and O. Martius, 2016: Regional-scale jet waviness modulates the occurrence of midlatitude weather extremes. *Geophys. Res. Lett.*, **43**, 10 989–10 997, https://doi.org/10.1002/2016GL070944.

Screen, J. A., and I. Simmonds, 2013: Exploring links between Arctic amplification and mid-latitude weather. *Geophys. Res. Lett.*, **40**, 959–964, https://doi.org/10.1002/grl.50174.

——, and ——, 2014: Amplified mid-latitude planetary waves favour particular regional weather extremes. *Nat. Climate Change*, **4**, 704–709, https://doi.org/10.1038/nclimate2271.

Seidel, D. J., and W. J. Randel, 2006: Variability and trends in the global tropopause estimated from radiosonde data. *J. Geophys. Res.*, **111**, D21101, https://doi.org/10.1029/2006JD007363.

Serreze, M. C., A. P. Barrett, J. C. Stroeve, D. N. Kindig, and M. M. Holland, 2009: The emergence of surface-based Arctic amplification. *Cryosphere*, **3**, 11–19, https://doi.org/10.5194/tc-3-11-2009.

Shaw, T. A., and Coauthors, 2016: Storm track processes and the opposing influences of climate change. *Nat. Geosci.*, **9**, 656–664, https://doi.org/10.1038/ngeo2783.

Sinclair, V. A., M. Rantanen, P. Haapanala, J. Räisänen, and H. Järvinen, 2020: The characteristics and structure of extra-tropical cyclones in a warmer climate. *Wea. Climate Dyn.*, **1**, 1–25, https://doi.org/10.5194/wcd-1-1-2020.

Sun, X., and Coauthors, 2022: Enhanced jet stream waviness induced by suppressed tropical Pacific convection during boreal summer. *Nat. Commun.*, **13**, 1288, https://doi.org/10.1038/s41467-022-28911-7.

Tamarin, T., and Y. Kaspi, 2016: The poleward motion of extra-tropical cyclones from a potential vorticity tendency analysis. *J. Atmos. Sci.*, **73**, 1687–1707, https://doi.org/10.1175/JAS-D-15-0168.1.

——, and ——, 2017a: Enhanced poleward propagation of storms under climate change. *Nat. Geosci.*, **10**, 908–913, https://doi.org/10.1038/s41561-017-0001-8.

——, and ——, 2017b: Mechanisms controlling the downstream poleward deflection of midlatitude storm tracks. *J. Atmos. Sci.*, **74**, 553–572, https://doi.org/10.1175/JAS-D-16-0122.1.

Tamarin-Brodsky, T., and N. Harnik, 2024: The relation between Rossby wave-breaking events and low-level weather systems. *Wea. Climate Dyn.*, **5**, 87–108, https://doi.org/10.5194/wcd-5-87-2024.

Thorncroft, C. D., B. J. Hoskins, and M. E. McIntyre, 1993: Two paradigms of baroclinic-wave life-cycle behaviour. *Quart. J. Roy. Meteor. Soc.*, **119**, 17–55, https://doi.org/10.1256/smsqj.50902.

Vallis, G. K., 2006: *Atmospheric and Oceanic Fluid Dynamics.* Cambridge University Press, 745 pp.

——, 2017: *Atmospheric and Oceanic Fluid Dynamics: Fundamentals and Large-Scale Circulation.* 2nd ed. Cambridge University Press, 946 pp.

Wallace, J. M., I. M. Held, D. W. J. Thompson, K. E. Trenberth, and J. E. Walsh, 2014: Global warming and winter weather. *Science*, **343**, 729–730, https://doi.org/10.1126/science.343.6172.729.

Wolf, G., D. J. Brayshaw, N. P. Klingaman, and A. Czaja, 2018: Quasi-stationary waves and their impact on European weather and extreme events. *Quart. J. Roy. Meteor. Soc.*, **144**, 2431–2448, https://doi.org/10.1002/qj.3310.

Woollings, T., and Coauthors, 2018: Blocking and its response to climate change. *Curr. Climate Change Rep.*, **4**, 287–300, https://doi.org/10.1007/s40641-018-0108-z.

Yuval, J., and Y. Kaspi, 2020: Eddy activity response to global warming–like temperature changes. *J. Climate*, **33**, 1381–1404, https://doi.org/10.1175/JCLI-D-19-0190.1.